JWST/NIRCam $4-5\,\mu\mathrm{m}$ Imaging of the Giant Planet AF Lep b

Kyle Franson , ** William O. Balmer , 2,3,† Brendan P. Bowler , Laurent Pueyo , Yifan Zhou , Emily Rickman , 5 Zhoujian Zhang (张周健) , 6,‡ Sagnick Mukherjee , 7 Tim D. Pearce , 8

Daniella C. Bardalez Gagliuffi , 9,10 Lauren I. Biddle , Timothy D. Brandt, Rachel Bowens-Rubin , 7

Justin R. Crepp , 11 James W. Davidson, Jr. , 4 Jacqueline Faherty , 10 Christian Ginski , 12

Elliott P. Horch , 13, § Marvin Morgan , Caroline V. Morley , Marshall D. Perrin , 3

Aniket Sanghi , 14, * Maïssa Salama , 7 Christopher A. Theissen , 15 Quang H. Tran , 1 and Trevor N. Wolf , 16

¹ Department of Astronomy, The University of Texas at Austin, Austin, TX 78712, USA ²Department of Physics & Astronomy, Johns Hopkins University, 3400 N. Charles Street, Baltimore, MD 21218, USA ³Space Telescope Science Institute, 3700 San Martin Dr, Baltimore, MD 21218, USA ⁴Department of Astronomy, University of Virginia, 530 McCormick Road, Charlottesville, VA 22904, USA ⁵ European Space Agency (ESA), ESA Office, Space Telescope Science Institute, 3700 San Martin Dr, Baltimore, MD 21218, USA ⁶ Department of Astronomy & Astrophysics, University of California, Santa Cruz, CA 95064, USA ⁷ Department of Astronomy & Astrophysics, University of California, Santa Cruz, CA 95064, USA ⁸ Department of Physics, University of Warwick, Gibbet Hill Road, Coventry, CV4 7AL, UK ⁹Department of Physics & Astronomy, Amherst College, 25 East Drive, Amherst, MA 01003, USA ¹⁰ American Museum of Natural History, 200 Central Park West, New York, NY 10024, USA ¹¹Department of Physics, University of Notre Dame, 225 Nieuwland Science Hall, Notre Dame, IN 46556, USA ¹²School of Natural Sciences, Center for Astronomy, University of Galway, Galway, H91 CF50, Ireland ¹³ Department of Physics, Southern Connecticut State University, 501 Crescent Street, New Haven, CT 06515, USA ¹⁴Department of Astronomy, California Institute of Technology, 1200 E. California Boulevard, Pasadena, CA 91125, USA ¹⁵Center for Astrophysics and Space Sciences, University of California, San Diego, 9500 Gilman Drive, La Jolla, CA 92093, USA ¹⁶Department of Aerospace Engineering and Engineering Mechanics, The University of Texas at Austin, Austin, TX 78712, USA

ABSTRACT

With a dynamical mass of 3 $M_{\rm Jup}$, the recently discovered giant planet AF Lep b is the lowest-mass imaged planet with a direct mass measurement. Its youth and spectral type near the L/T transition make it a promising target to study the impact of clouds and atmospheric chemistry at low surface gravities. In this work, we present JWST/NIRCam imaging of AF Lep b. Across two epochs, we detect AF Lep b in F444W (4.4 μ m) with S/N ratios of 9.6 and 8.7, respectively. At the planet's separation of 320 mas during the observations, the coronagraphic throughput is \approx 7%, demonstrating that NIRCam's excellent sensitivity persists down to small separations. The F444W photometry of AF Lep b affirms the presence of disequilibrium carbon chemistry and enhanced atmospheric metallicity. These observations also place deep limits on wider-separation planets in the system, ruling out 1.1 $M_{\rm Jup}$ planets beyond 15.6 au (0.58), 1.1 $M_{\rm Sat}$ planets beyond 27 au (1), and 2.8 $M_{\rm Nep}$ planets beyond 67 au (2.5). We also present new Keck/NIRC2 L' imaging of AF Lep b; combining this with the two epochs of F444W photometry and previous Keck L' photometry provides limits on the long-term 3–5 μ m variability of AF Lep b on months-to-years timescales. AF Lep b is the closest-separation planet imaged with JWST to date, demonstrating that planets can be recovered well inside the nominal (50% throughput) NIRCam coronagraph inner working angle.

1. INTRODUCTION

- * NSF Graduate Research Fellow
- [†] Johns Hopkins University George Owen Fellow
- [‡] NASA Sagan Fellow
- § Adjunct Astronomer, Lowell Observatory

The atmospheres of gas giants and brown dwarfs undergo dramatic changes as they cool and evolve. Thick clouds suspended in the atmospheres of warmer L-dwarfs break up and sink below the photosphere at the L/T transition, yielding the clear atmospheres of cooler T dwarfs (Tsuji et al. 1996; Burrows et al. 2001; Knapp et al. 2004). Coinciding with this transition,

near-infrared (NIR) colors shift blueward and the dominant carbon-bearing molecule shifts from carbon monoxide (CO) to methane (CH₄), causing the characteristic sharp CH₄ absorption features of T dwarfs (Oppenheimer et al. 1995; Kirkpatrick 2005). For field objects, the L/T transition occurs at $T_{\rm eff} \sim 1200-1400\,{\rm K}$ (Filippazzo et al. 2015; Sanghi et al. 2023). However, young, low-gravity giant planets and brown dwarfs follow a different path, retaining clouds, red NIR colors, and CO absorption to much lower effective temperatures than their field-age brown dwarf counterparts (e.g., Chauvin et al. 2004; Marois et al. 2008; Bowler et al. 2010, 2013; Faherty et al. 2016; Liu et al. 2016). The retention of photospheric condensates may be caused by the dependence of cloud base pressure and particle size with surface gravity (Marley et al. 2012), while the preservation of CO and lack of CH₄ at NIR wavelengths points to disequilibrium carbon chemistry caused by strong vertical mixing in low-surface-gravity atmospheres (e.g., Hinz et al. 2010; Barman et al. 2011; Konopacky et al. 2013; Skemer et al. 2012, 2014). However, the dearth of imaged planets spanning the L/T transition limits understanding this change in detail.

AF Lep b is a recent addition to the census of young imaged planets. It was independently discovered by three groups searching for planets around stars with astrometric accelerations between Hipparcos and Gaia (Franson et al. 2023; De Rosa et al. 2023; Mesa et al. 2023). With a mass of $2.8^{+0.6}_{-0.5} M_{\text{Jup}}$ and semi-major axis of $8.2^{+1.3}_{-1.7}$ au (Zhang et al. 2023), AF Lep b is the lowest-mass directly imaged planet with a dynamical mass measurement. The system is a member of the β Pic moving group with an age of $24 \pm 3 \,\mathrm{Myr}$ (Bell et al. 2015). It resides at the L/T transition, with a luminosity between that of the early-L dwarf β Pic b (Lagrange et al. 2010; Bonnefov et al. 2014) and the mid-to-late T dwarf 51 Eri b (Macintosh et al. 2015; Rajan et al. 2017). There are signs of methane absorption in the K-band spectral shape of AF Lep b (De Rosa et al. 2023) and evidence for an enhancement in atmospheric metallicity (Zhang et al. 2023; Palma-Bifani et al. 2024), similar to Jupiter and Saturn (Atreya et al. 2003; Flasar et al. 2005). Based on AF Lep b's bolometric luminosity and dynamical mass, Franson et al. (2023), Zhang et al. (2023), and Zhang (2024) found hints of differential ages between the planet and its host star, which may represent the first direct evidence of delayed formation by a few Myr as would be expected for a planet forming through core accretion. The system also hosts an unresolved debris disk with an estimated separation of 46 ± 9 au (Pawellek et al. 2021; Pearce et al. 2022). Using dynamical arguments, Pearce et al. (2022) found that a

 $1.1\pm0.2\,M_{\mathrm{Jup}}$ planet at $35\pm6\,\mathrm{au}$ is consistent with truncating the inner edge of this debris disk—perhaps a sign of an outer planet beyond AF Lep b in the system—although it could also be explained by multiple small planets or by AF Lep b forming at wider separations and migrating inward.

Here we present the results of a Director's Discretionary Time program (Program ID 4558; Co-PIs Franson, Balmer) to image AF Lep b with the Near-Infrared Camera (NIRCam; Rieke et al. 2005, 2023) on JWST (Gardner et al. 2006, 2023). At its current separation of \sim 320 mas (2.3 λ/D in F444W) and contrast of \sim 10 mag in thermal wavelengths (Franson et al. 2023), AF Lep b is a challenging object to recover with JWST. However, the recent successful detection of HR 8799 e with the Mid-infrared Instrument (MIRI; Boccaletti et al. 2023) and outstanding coronagraphic performance of NIRCam (e.g., Girard et al. 2022; Kammerer et al. 2022, 2024; Carter et al. 2023; Lawson et al. 2023) open the possibility of high-contrast imaging below the nominal (50% throughput) coronagraph inner working angle. Extending the Spectral Energy Distribution (SED) of AF Lep b to $4-5 \,\mu\mathrm{m}$ provides an opportunity to search for signs of disequilibrium chemistry and metallicity enhancement by sampling the $4.3 \,\mu\mathrm{m}$ CO₂ and $4.6 \,\mu\mathrm{m}$ CO absorption bands. Additionally, NIRCam imaging enables a deep search for other planets in the system at wider separations including a potential sculptor of the debris disk. Finally, we also report new Keck/NIRC2 L' imaging as part of a search for variability from 3–5 μ m over a baseline of 2.1 years.

2. OBSERVATIONS AND DATA REDUCTION

2.1. JWST/NIRCam Imaging

We obtained F200W $(1.755-2.227 \,\mu\text{m})$, F356W $(3.135-3.981 \,\mu\text{m})$, and F444W $(3.881-4.982 \,\mu\text{m})$ JWST/NIRCam imaging of AF Lep on UT 2023 October 12. This dataset was affected by a severe mirror "tilt event" shortly before the observations. Tilt events are occassional abrupt changes in the position of one or more mirror segments thought to arise from structural microdynamics within the telescope (Rigby et al. 2023). The wavefront stability is measured with NIRCam approximately every two days (Acton et al. 2012; McElwain et al. 2023). At UT 2023 October 12 06:53:15.4, 14 minutes before the imaging sequence, NIRCam measured a total wavefront error (WFE) of 96.2 nm rms, compared to a baseline of 69.2 nm rms on UT 2023 October 5. At the time, this was the highest WFE since October 2022 and the second highest since commissioning. Because of the potential impact of this tilt event on the dataset, a second set of observations were obtained on UT January

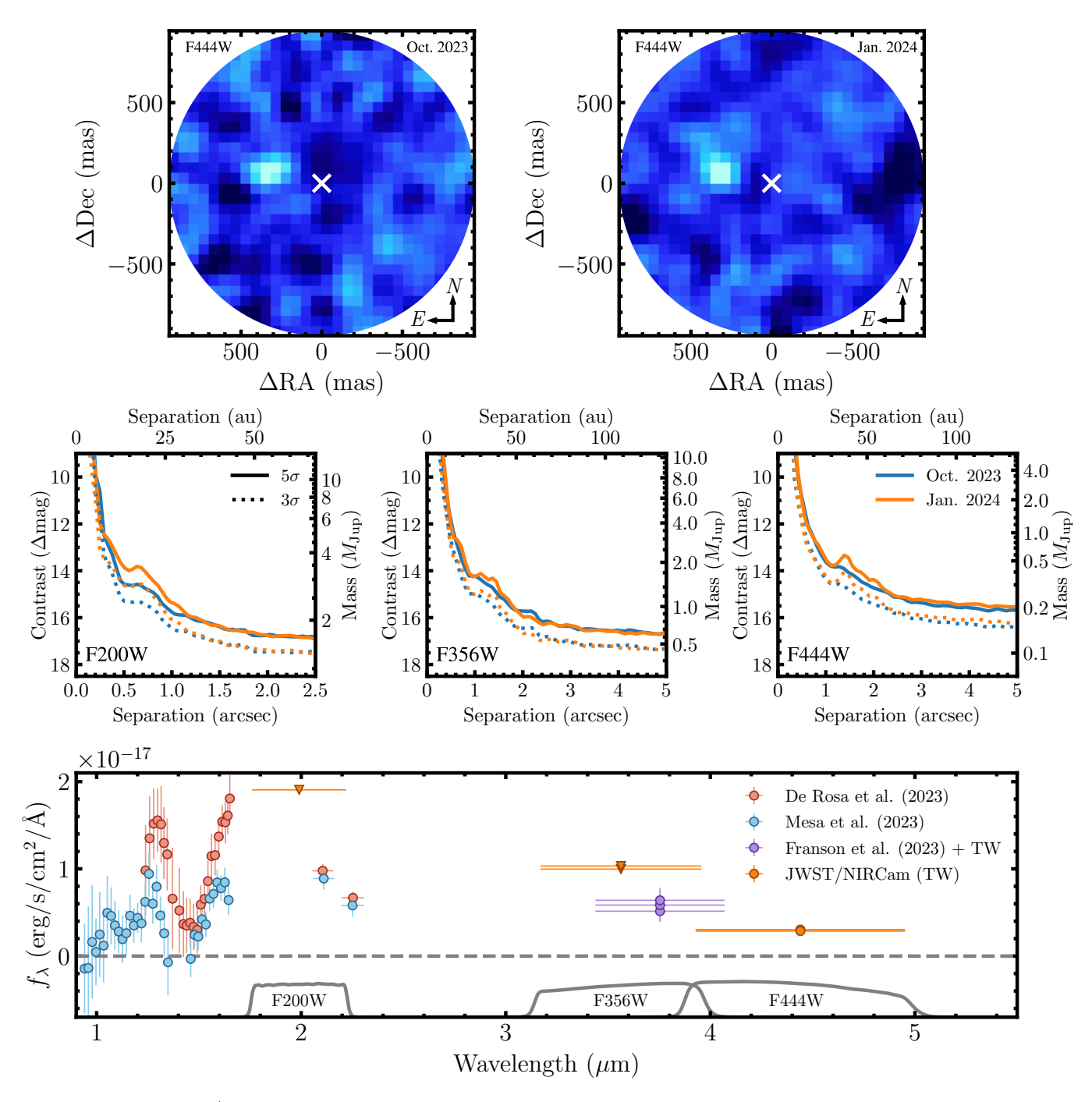


Figure 1. Top: JWST/NIRCam imaging of AF Lep b in F444W. Each image is oriented so north is up and east is to the left. To average over pixel-to-pixel noise, the images are convolved with a Gaussian filter with a standard deviation of 1 pixel. AF Lep b is recovered with a S/N of 9.6σ in October 2023 and 8.7σ in January 2024 at 4.44 μm. Middle: 5σ (solid) and 3σ (dotted) contrast curves in F200W (left), F356W (middle), and F444W (right). Blue lines denote contrast curves for the October 2023 observations, while orange lines correspond to the January 2024 observations. Each right axis shows corresponding model-inferred masses from ATMO-2020 and Linder et al. (2019). F444W provides the deepest mass limits, ruling out Saturn-mass planets beyond 1" (27 au) and $0.14\,M_{\rm Jup}=2.5\,M_{\rm Nep}$ planets beyond 2".5 (67 au). Bottom: Spectral energy distribution of AF Lep b from 1–5 μm. SPHERE IRDIS photometry and IFS spectroscopy from De Rosa et al. (2023) and Mesa et al. (2023) are shown in red and blue, respectively. Keck/NIRC2 L' photometry from Franson et al. (2023) and this work are shown in purple. Our new JWST/NIRCam F444W photometry is shown in orange with 5σ upper limits denoted by upside-down triangles. Note that the January 2024 F200W upper limit of $2.8 \times 10^{-17}\,\rm erg/s/cm^2/\mathring{A}$ is outside the bounds of this figure.

12 2024. These observations were acquired under nominal wavefront conditions: a WFE of 67.2 nm rms was measured on UT 2024 January 12 19:55:41.5 and 66.2 nm rms on UT 2024 January 15 10:23:19.7. Despite the tilt event, we elect to analyze both datasets in this work because the October sequence retains two advantages over the January data: AF Lep b is at a slightly wider separation and the star is better centered behind the coronagraph, as detailed below.

Each sequence consists of two roll angles centered on AF Lep immediately followed by deep imaging of the reference star HD 33093. This approach facilitates both Angular Differential Imaging (ADI; Liu 2004; Marois et al. 2006) and Reference Star Differential Imaging (RDI; Lafrenière et al. 2009). HD 33093 was selected as the reference star for this program based on its similar magnitude, spectral type, and angular proximity to AF Lep. 12 Each epoch is executed as a non-interrutible sequence to minimize wavefront drift. The roll angles are separated by 10.0° in each sequence. All imaging is taken with the 335R occulting mask (Krist et al. 2010), which has a smooth transmission function with an Inner Working Angle (IWA) of 0".63. To ensure a sufficient diversity of reference PSFs and to mitigate the impact of target acquisition errors, the 9-POINT-CIRCLE dither pattern is used for the reference star observations. F200W imaging is taken simultaneously with F356W and F444W imaging using the NIRCam dichroic. We use the SUB320A335R subarray to minimize readout times. This gives a field of view of $20'' \times 20''$ in F356W/F444W and $10'' \times 10''$ in F200W. In each sequence, we obtained 35 integrations of five groups in the SHALLOW4 readout pattern for each filter combination (F200W/F356W and F200W/F444W) and roll angle of AF Lep. For the first epoch in October 2023, the reference star observations consist of 14 integrations in F200W/F444W and 13 integrations in F200W/F356W of five SHALLOW4 groups per dither position. For the second sequence in January 2024, 15 integrations of the reference star are obtained in each dither position and filter combination. For both sequences, the total exposure time on AF Lep is 62.4 min in F200W and 31.2 min in F356W and F444W. The total exposure time on the reference star in the October 2023 observations is 108.3 min in F200W, 52.2 min in F356W, and 56.2 min in F444W. For the January 2024 observations, the reference star exposure time is 120.4 min in F200W and 60.2 min in both F356W and F444W.

We process uncalibrated Stage 0 files into Stage 1 and Stage 2 data products using spaceKLIP³ (Kammerer et al. 2022), which makes use of the jwst pipeline⁴ (Bushouse et al. 2023) for basic data processing steps with modifications for coronagraphic imaging reduction as detailed in Carter et al. (2023). Following Carter et al. (2023), we do not carry out dark current subtraction, as the NIRCam dark current calibration data contains a large number of hot pixels, cosmic rays, and persistence features that result in reduced sensitivity when included. We use a jump detection threshold of four when reducing the up-the-ramp uncalibrated data. In this step spaceKLIP applies a 1/f noise correction: a master slope image is subtracted from each ramp image to produce a residual that is modeled using a Savitzky-Golav filter. This model (which approximates the 1/fnoise) is then removed from each ramp frame (see e.g., Rebollido et al. 2024). Following processing into Stage 2 calibrated products, we perform standard pixel cleaning procedures for NIRCam high-contrast imaging. Pixels flagged as poor data quality by the jwst pipeline together with 3σ outliers are replaced with the median of neighboring pixels. We also identify anomalous pixels by flagging pixels with significant temporal flux variations between integrations. Pixels brighter than $1 \,\mathrm{MJy \, sr^{-1}}$ or fainter than 20% of the brightest value for a given pixel position are replaced with the median value of the pixel in the exposure sequence. The position of the star behind the coronagraph is determined by fitting a model coronagraphic PSF from webbpsf_ext.⁵ We find that AF Lep is better centered in the October 2023 imaging $(\approx 1.5 \text{ mas offset})$ than the January 2024 imaging (≈ 20) mas offset). The January 2024 centering offset is large

 $^{^1}$ HD 33093 has a spectral type of GoIV (Gray et al. 2006) and W1-band magnitude of $4.43\pm0.09\,\mathrm{mag}$ (Cutri et al. 2012). This closely matches the spectral type (F8V; Gray et al. 2006) and magnitude ($W1\text{=}4.92\pm0.07\,\mathrm{mag}$; Cutri et al. 2012) of AF Lep. The angular separation between the stars is 4°8. HD 33093 also has a Renormalised Unit Weght Error (RUWE; Lindegren 2018) in Gaia DR3 of 1.047, fraction of double transits parameter (IFDsp; see e.g., Tokovinin 2023) of 0, and lacks a significant astrometric acceleration in the Hipparcos-Gaia Catalog of Accelerations (HGCA; Brandt 2021), all of which point to the star being single.

² To ensure that the reference star is not a close visual binary, we obtained diffraction-limited imaging of HD 33093 on UT 2023 September 1 using the Differential Speckle Survey Instrument (DSSI, Horch et al. 2009), a visible-light speckle camera currently on the Astrophysical Research Consortium 3.5-m telescope at Apache Point Observatory (See Davidson et al. 2024). HD 33093 was also observed with VLT/SPHERE (Beuzit et al. 2019) on UT 2023 October 16. The star appeared single in both datasets.

 $^{^3}$ We use version 2 of the development branch of ${\tt spaceKLIP}$ (commit # f64258 d).

⁴ We use pipeline version CAL_VAR = 1.12.5 and calibration reference data jwst_1183.pmap.

⁵ https://github.com/JarronL/webbpsf_ext

but not an abnormal deviation compared to the target acquisition performance of NIRCam with the 335R mask ($\sigma \approx 15\,\mathrm{mas}^6$).

We carry out PSF subtraction with spaceKLIP, which uses the Karhunen-Loève Image Projection (KLIP; Soummer et al. 2012) algorithm implemented in pyklip (Wang et al. 2015) to model and subtract the host-star PSF. The following combination of parameters effectively suppresses residual speckle noise for each filter: 100 KL modes, four annuli, and three subsections, utilizing both ADI and RDI for reference frames. Figure 1 shows the final PSF-subtracted images in F444W. AF Lep b is detected in F444W at S/N ratios of 9.6 and 8.7 for the October 2023 and January 2024 epochs, respectively. Here, S/N is measured by comparing the flux in a circular aperture at the position of AF Lep b against the noise level estimated by ten non-overlapping apertures at the same separation. To correct for small-sample statistics at small separations, we adopt the Student's tdistribution with equivalent false-alarm probabilities to our Gaussian significance levels following Mawet et al. (2014). The comparable detection significance between the two datasets despite the higher WFE in the October 2023 dataset may be due to the larger centering offset in the January 2024 sequence. AF Lep b is not recovered at a significant level (above 5σ) in other filters. No other significant sources are detected in the full-frame images.8

To measure the astrometry and photometry of AF Lep b, we use the KLIP forward modeling (KLIP-FM; Pueyo 2016) framework implemented in spaceKLIP and pyKLIP. This approach yields a flexible forward model that incorporates the distortions that KLIP introduces to a planet's PSF. This can then be fit to a given source in a post-processed image within a Bayesian framework (see e.g., Wang et al. 2016). We employ the emcee affine-invariant Markov-chain Monte Carlo (MCMC) ensemble sampler (Foreman-Mackey et al. 2013) to simultaneously fit the planet separation, position angle, and flux ratio. The PSF model is produced by webbpsf (Perrin et al. 2012, 2014). A total of 50 walkers over 1.5×10^4 total steps (300 per walker) are used to sample the three model parameter posteriors. We dis-

card the first 100 steps of each chain as burn-in. As speckle noise is correlated at the separation of AF Lep b, we model the noise distribution via a Gaussian process with a Matérn ($\nu=3/2$) kernel following Wang et al. (2016). This increases the photometric uncertainties from $\approx \pm 0.10\,\mathrm{mag}$ to $\approx \pm 0.15\,\mathrm{mag}$ compared to assuming uncorrelated noise (the "diagonal kernel" in spaceKLIP).

Astrometric and photometric uncertainties are determined from the standard deviation of the MCMC chains. Following Carter et al. (2023), the adopted astrometric measurements incorporate a 6.3 mas (0.1 pixel) absolute centering uncertainty added in quadrature to account for the precision of the measurement of the host-star position behind the mask. Additionally, a 1.5% uncertainty is added to the contrast uncertainties in quadrature to reflect the absolute flux calibration accuracy of NIRCam.⁹ To correct for the throughput of the coronagraph, we use NIRCam MASK335R throughput maps generated through the procedure detailed in Carter et al. (2023) and included in spaceKLIP.

The resulting astrometry and photometry are shown in Table 1. For the October 2023 imaging, we measure a separation $\rho = 308 \pm 18 \,\mathrm{mas}$, position angle $\theta = 73^{\circ}.6 \pm 18 \,\mathrm{mas}$ 2°.4, and F444W contrast $\Delta_{\rm F444W} = 9.98 \pm 0.15$ mag. For the January 2024 observations, we measure $\rho = 313 \pm$ 16 mas, $\theta = 76^{\circ}.2 \pm 2^{\circ}.7$, and $\Delta_{\text{F444W}} = 10.05 \pm 0.17$ mag. At the position of AF Lep b, 92% (October 2023) and 94% (January 2024) of the flux is attenuated by the coronagraph. To convert contrasts into apparent magnitudes and flux densities, we synthesize photometry of the host star by scaling a F8V (Gray et al. 2006) BOSZ (Bohlin et al. 2017) stellar model to photometry of AF Lep from Gaia DR3 (Gaia Collaboration et al. 2022), Tycho-2 (Høg et al. 2000), 2MASS (Skrutskie et al. 2006), and WISE (Cutri et al. 2012). This produces apparent magnitudes of $m_{\rm F444W} = 14.93 \pm 0.15 \,\rm mag$ and $m_{\rm F444W} = 15.00 \pm 0.17\,{\rm mag}$ and flux densities of $f_{\rm F444W} = (3.0 \pm 0.4) \times 10^{-18} \, {\rm erg/s/cm^2/\AA} \, {\rm and} \, f_{\rm F444W} =$ $(2.9 \pm 0.4) \times 10^{-18} \,\mathrm{erg/s/cm^2/Å}$.

We measure 5σ upper limits in F200W and F356W through injection-recovery. Synthetic sources generated with webbpsf are injected at the same separation as AF Lep b across ≈ 13 non-overlapping position angles. The S/N of each injected source is then measured by the same method as above, here masking both the position of AF Lep b and the synthetic source. The injected flux is then adjusted to produce a S/N of 5σ . The mean

 $^{^{6}\} https://jwst-docs.stsci.edu/jwst-calibration-status/nircam-calibration-status/nircam-coronagraphy-calibration-status$

⁷ See Appendix A for F356W and F200W imaging.

⁸ An artifact appears in the October 2023 F444W reduced images at a separation of 5".7 and position angle of 27°. This appears to be caused by a cosmic ray hitting the detector between rolls, causing a "snowball" artifact that is missed by jump detection (see e.g., Bagley et al. 2023). The artifact is removed when the first five integrations of the second roll angle are excluded.

⁹ https://jwst-docs.stsci.edu/jwst-calibration-status/nircam-calibration-status/nircam-coronagraphy-calibration-status

Date	Epoch	Instrument	Filter	ρ	θ	$\Delta_{ m mag}$	$f_{\lambda} \times 10^{-18}$
(UT)	(UT)			(mas)	(°)	(mag)	$(\rm erg/s/cm^2/\mathring{A})$
2023 Oct 12	2023.779	JWST/NIRCam	F444W	308 ± 18	73.6 ± 2.4	9.98 ± 0.15	3.0 ± 0.4
$2023 \ \mathrm{Oct} \ 12$	2023.779	JWST/NIRCam	F356W			>9.6 ^a	$< 10^{a}$
$2023 \ \mathrm{Oct} \ 12$	2023.779	JWST/NIRCam	F200W			$> 11.2^{a}$	$< 19^{a}$
$2024~\mathrm{Jan}~14$	2024.038	JWST/NIRCam	F444W	313 ± 16	76.2 ± 2.7	10.05 ± 0.17	2.9 ± 0.4
$2024~\mathrm{Jan}~14$	2024.038	JWST/NIRCam	F356W			>9.5 ^a	$< 10^{a}$
$2024~\mathrm{Jan}~14$	2024.038	JWST/NIRCam	F200W			$> 10.8^{a}$	$< 28^{a}$
$2024~\mathrm{Jan}~30$	2024.080	Keck/NIRC2	L'	300 ± 7	80.6 ± 1.2	9.90 ± 0.25	6.4 ± 1.4

Table 1. New Astrometry and Photometry of AF Lep b

injected flux across all position angles is taken as the 5σ upper limit. These upper limits are shown in Table 1. We measure F200W upper limits of >11.2 mag and >10.8 mag and F356W upper limits of >9.6 mag and >9.5 mag for the October and Januaray imaging, respectively. These correspond to flux densities of $<19\times10^{-18}\,\mathrm{erg/s/cm^2/\mathring{A}}$ and $<28\times10^{-18}\,\mathrm{erg/s/cm^2/\mathring{A}}$ in F200W and $<10\times10^{-18}\,\mathrm{erg/s/cm^2/\mathring{A}}$ and $<10\times10^{-18}\,\mathrm{erg/s/cm^2/\mathring{A}}$ in F356W for the two epochs.

We compute 3σ and 5σ contrast curves with spaceKLIP for each filter and epoch. Across a range of separations, the noise level is measured in annuli within the PSF-subtracted images while masking the position of AF Lep b. The Mawet et al. (2014) correction for small-sample statistics at small separations is then applied and the noise level is corrected for coronagraphic and algorithmic throughput. Algorithmic throughput is determined by performing injection-recovery with synthetic PSFs generated with webbpsf. Contrast curves for each filter are shown in the middle row of Figure 1.

2.2. Keck/NIRC2 Imaging

We obtained high-contrast imaging of AF Lep on UT January 30 2024 with the NIRC2 camera at W.M. Keck Observatory using natural guide star adaptive optics (Wizinowich 2013). Our observations are taken in pupil-tracking mode to facilitate ADI. No coronagraph is used for our sequence. Each science frame consists of 100 coadds of an integration time of $0.054\,\mathrm{s}$. To minimize read-out times, we use a subarray of 512×512 pixels (5".1 \times 5".1). Throughout the sequence, we also periodically take short frames with a smaller subarray (192 \times 248 pixels) to obtain unsaturated images of the host star for flux calibration. These PSF frames each have 100 coadds of 0.017 s. The total on-source inte-

gration time is 90.8 min, amounting to 99.9° of frame rotation.

Basic data reduction steps follow Franson et al. (2022). After flat-fielding and subtracting darks, we identify and remove cosmic rays using L.A. Cosmic (van Dokkum 2001). To correct for geometric distortions, we apply the Service et al. (2016) solution using rain, 10 which implements the Drizzle image recombination algorithm (Fruchter & Hook 2002) in Python. Frames are registered by fitting two-dimensional Gaussians to determine the center of each PSF and then all images are aligned to the sub-pixel level using a third-order spline. PSF subtraction is carried out using pyKLIP (Wang et al. 2015) with the following parameters: 20 KL modes, three annuli, four subsections, and a movement parameter of one. We recover AF Lep b at a S/N of 6.6σ .

Astrometry and photometry are measured with pyKLIP using the KLIP-FM framework (Pueyo 2016; Wang et al. 2016). We use emcee (Foreman-Mackey et al. 2013) to sample the companion parameter space with 100 walkers and 1.6×10^5 total steps (1600 steps per walker). The first 25% of each chain is discarded as burn-in. Following Franson et al. (2022), astrometric uncertainties incorporate the standard deviation of the separation and position angle posterior distributions, the uncertainty on the Service et al. (2016) distortion solution of $\sigma_d = 1 \,\mathrm{mas}$, the plate scale uncertainty, and the north alignment uncertainty added in quadrature. Our contrast uncertainty is taken from the standard deviation of the flux ratio posterior. We measure a separation of $300 \pm 7 \,\mathrm{mas}$, position angle of $80^{\circ}.6 \pm 1^{\circ}.2$, and L' contrast of 9.90 ± 0.25 mag. Incorporating the W1 magnitude of AF Lep A (4.92 ± 0.07) ;

 $[^]a5\sigma$ limits measured through injection-recovery at the separation of AF Lep b.

¹⁰ https://github.com/jsnguyen/rain

Cutri et al. 2012), this contrast corresponds to an apparent magnitude of 14.83 ± 0.26 mag, an absolute magnitude of 12.68 ± 0.26 mag, and a flux density $f_{\lambda} = (6.4 \pm 1.4) \times 10^{-18} \, \mathrm{erg/s/cm^2/\mathring{A}}$.

3. RESULTS

3.1. Limits on Outer Planets

To convert the NIRCam contrast curves to mass limits, we follow Carter et al. (2021) in combining the ATMO-2020 hot-start evolutionary models (Phillips et al. 2020), which span $0.5-75 M_{\text{Jup}}$, and the BEX models (Linder et al. 2019), which span $0.16-2\,M_{\mathrm{Jup}}$. To ensure consistency with the BEX models, which do not incorporate disequilibrium chemistry, the ATMO-2020 grid in chemical equilibrium is adopted. Since ATMO-2020 models are cloudless, we select the cloudless, solarmetallicity BEX grid computed via petitCODE (Mollière et al. 2015). Linder et al. (2019) computed evolutionary tracks with three prescriptions for the initial luminosity of the planet: a nominal post-formation luminosity based on the output of a population synthesis model of planet formation (Mordasini et al. 2017), a "hotter-start" scenario where the initial luminosity is increased by an order of magnitude, and a "colderstart" scenario where the initial luminosity is decreased by an order of magnitude. We adopt the nominal case, which has the most extensive set of evolutionary tracks. Note that above ages of 1 Myr, the difference between the nominal and hotter-start cases is minimal (Linder et al. 2019). Each model grid is interpolated using the species package (Stolker et al. 2020) to generate modelinferred masses as a function of contrast within each filter, assuming an age of 24 Myr for AF Lep based on the β Pic moving group age (24 ± 3 Myr; Bell et al. 2015). At contrasts covered by both model grids, we take the average of the two masses.

Figure 1 shows our mass limits as a function of separation. In the background-limited regime, we are sensitive to Jupiter-mass planets in F200W (1.7 M_{Jup} beyond 3"), sub-Jupiter-mass planets in F356W $(0.75M_{\text{Jup}})$ beyond 2''), and sub-Saturn-mass planets in F444W (0.2 $M_{\text{Jup}} =$ $3.6M_{\text{Nep}}$ beyond 2"). Our F444W imaging is most sensitive to low-mass planets. We rule out planets above masses of $1.9 M_{\text{Jup}}$ at 0.75 (13 au), $0.34 M_{\text{Jup}} = 1.1 M_{\text{Sat}}$ at 1" (27 au), $0.20 M_{\text{Jup}} = 0.65 M_{\text{Sat}}$ at 2" (67 au), and $0.15 M_{\text{Jup}} = 0.51 M_{\text{Sat}} = 2.8 M_{\text{Nep}}$ from 2".5 to 5" (67–134 au). If instead, we assume cold-start formation conditions, the Linder et al. (2019) models produce mass limits of $0.44 M_{\text{Jup}}$, $0.26 M_{\text{Jup}}$, and $0.24 M_{\text{Jup}}$ at 1", 2", and 2"5, respectively. The cold-start grid only spans $0.06-1\,M_{\mathrm{Jup}}$; at 0".5, the F444W contrast is outside the bounds of the grid.

AF Lep hosts a debris disk with an estimated separation of 46 ± 9 au, inferred from infrared excess (Pawellek et al. 2021; Pearce et al. 2022), raising the possibility that one or more planets are sculpting its inner edge. Using dynamical arguments, Pearce et al. (2022) determined that the minimum mass for a single giant planet to truncate the debris disk is $1.1 \pm 0.2 M_{\rm Jup}$ at a semimajor axis of 35 ± 6 au. Other possibilities are that the inner edge is set by multiple smaller planets with masses as low as $0.09 \pm 0.03 \, M_{\rm Jup}$ or that AF Lep b formed closer to the disk and then migrated inwards. With JWST, we largely rule out the single, non-migrating planet scenario. The F444W imaging is sensitive to planet masses of $1.1\,M_{\rm Jup}$ beyond a projected separation of 0".58 (15.6 au) assuming hot-start formation, or $1 M_{\text{Jup}}$ beyond 0.64 (17.2 au) in the cold-start scenario. However, a sculpting planet could have been at an unfavorable phase in its orbit during our observations. To estimate the probability of this happening by chance, we employ a Monte Carlo approach by computing 10⁴ circular orbits with isotropic inclinations and semi-major axes drawn from the Pearce et al. (2022) prediction $(35 \pm 6 \,\mathrm{au})$. We find that planets on these orbits are beyond 0.58 95% of the time. If instead, we assume that the debris disk is coplanar with AF Lep b $(i = 55^{+8}_{-13})^{\circ}$; Zhang et al. 2023) and sample planet orbits from that inclination distribution, 90% of the orbits result in a planet at a projected separation beyond 0".58. The nondetection of an additional planet in the system therefore largely rules out the hypothesis that an additional giant planet is truncating the debris disk around AF Lep.

3.2. Atmospheric Modeling

The NIRCam detection of AF Lep b in F444W extends the planet's Spectral Energy Distribution (SED) into the $4-5\,\mu\mathrm{m}$ regime (see Figure 1, bottom row). In this section, we examine the impact of this additional photometry on the inferred atmospheric properties through two approaches. First, we compare the $3-5\,\mu\mathrm{m}$ SED against the predictions of grid-based models. We then perform a new atmospheric retrieval within the framework of Zhang et al. (2023), incorporating all published photometry and spectroscopy of AF Lep b.

3.2.1. Grid-based Model Comparison

The main spectral features from $3-5\,\mu\mathrm{m}$ for L and T dwarfs are the ν_3 fundamental absorption band of CH₄ from $\sim 3.0-3.8\,\mu\mathrm{m}$ and the $\nu = 1-0$ fundamental absorption band of CO from $\sim 4.4-5.0\,\mu\mathrm{m}$. The CO₂ ν_3 fundamental band may also contribute to absorption from $4.2-4.4\,\mu\mathrm{m}$. Combining the L' photometry of AF Lep b, which samples CH₄ absorption, with the F444W photometry, which samples CO and CO₂ absorption, thus

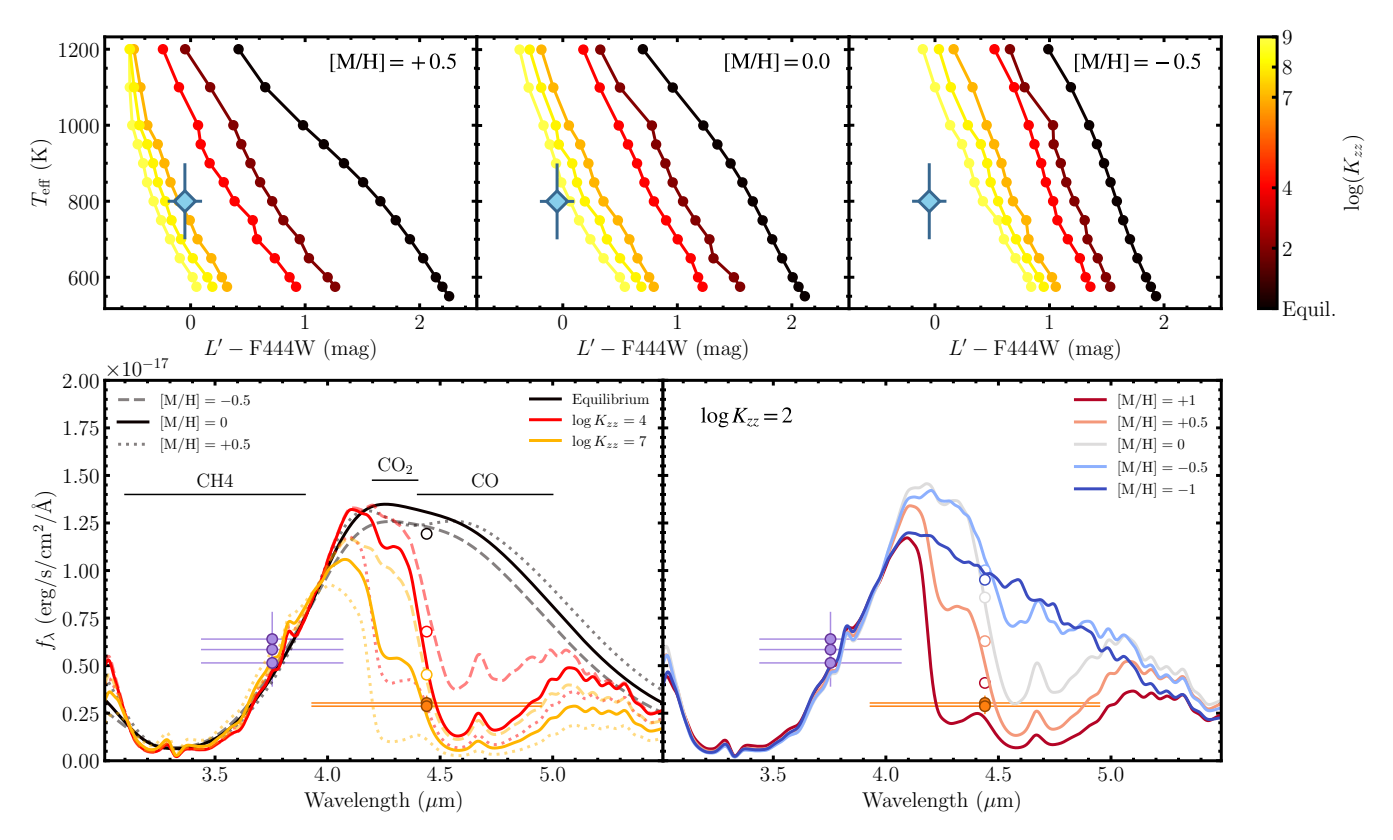


Figure 2. Top: $T_{\rm eff}$ vs. $L'-{\rm F444W}$ color of AF Lep b (blue diamond), compared against Sonora Elf-Owl (Mukherjee et al. 2024) and Bobcat (Marley et al. 2021) model atmospheres, varying metallicity and $\log K_{zz}$. Bobcat models (black) do not have $\log K_{zz}$ as a tunable parameter since they assume chemical equilibrium. Here, we include models with $\log g = 3.5\,{\rm dex}$ and solar C/O values. Bottom: SED of AF Lep b from $3-5\,\mu{\rm m}$. F444W photometry is shown in orange and L' photometry is shown in purple. The background tracks are Elf-Owl and Bobcat model atmospheres smoothed to R=100 and anchored to the weighted mean of the L' photometry. Open circles show synthesized F444W photometry from the model spectra. The left panel includes models spanning equilibrium chemistry to disequilibrium chemistry with $\log K_{zz}=7$ and metallicity from -0.5 to +0.5. The right panel includes Elf-Owl models with $\log K_{zz}=2$ and metallicity spanning a wider range of -1 to +1. Our F444W photometry is consistent with models that have a high $\log K_{zz}$ (more vigorous mixing) and $[{\rm Fe}/{\rm H}]=0$ or +0.5, or models with lower $\log K_{zz}$ (less vigorous mixing) and a super-solar metallicity ($[{\rm Fe}/{\rm H}]=1$). Equilibrium and sub-solar models are inconsistent with our photometry.

provides a means to constrain the planet's carbon chemistry and the presence of disequilibrium processes elevating its CO abundance. De Rosa et al. (2023) performed a similar exercise in the K-band, comparing the K1-K2 color of AF Lep b to other directly imaged planets, finding that AF Lep b has a color intermediate between that of red L-dwarf planets and 51 Eri b. This hints at the beginning of methane absorption in the atmosphere of AF Lep b.

The L'-F444W color of AF Lep b is -0.05 ± 0.15 mag. The sample of imaged exoplanets with L' and F444W photometry for direct comparison is limited to the midto-late L-dwarf planet HIP 65426 b (Chauvin et al. 2017), which has an L' - F444W color of -0.23 ± 0.14 mag (Cheetham et al. 2019; Carter et al. 2023), and the early L-dwarf planet β Pic b (Lagrange et al. 2010; Bonnefoy et al. 2014), which has an L' - F444W

color of 0.11 ± 0.08 mag (Currie et al. 2013; Kammerer et al. 2024). Bluer L'-F444W colors indicate CO absorption, while redder colors point to CH₄ absorption. To further contextualize this spectral slope, we compare the $3-5\,\mu\mathrm{m}$ photometry of AF Lep b against Sonora Bobcat (Marley et al. 2021) and Sonora Elf Owl (Mukherjee et al. 2024) model atmospheres. The Sonora Bobcat grid is computed assuming chemical equilibrium and cloudless atmospheres, varying metallicity, $\log g$, $T_{\rm eff}$, and C/O ratio. Sonora Elf Owl models extend Bobcat models with a self-consistent treatment of disequilibrium chemistry across a wide range of effective temperatures (275 to 2400 K), C/O ratios (0.22 to 1.24), and metallicities ([M/H]= -1.0 to +1.0). Disequilibrium chemistry from vertical mixing is parametererized by the eddy diffusion coefficient K_{zz} (Griffith & Yelle 1999), where high values of K_{zz} indicate strong

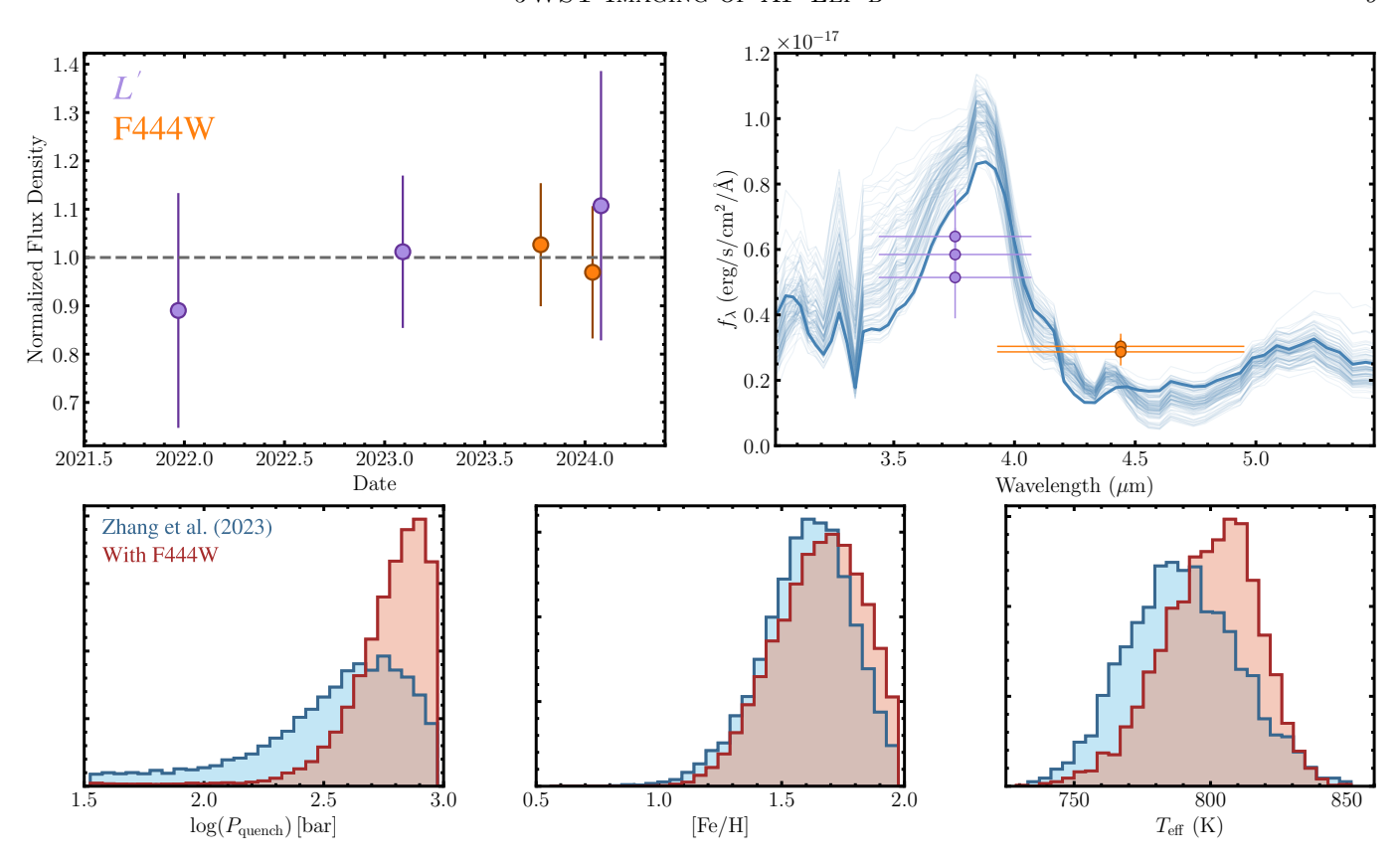


Figure 3. Top left: L' (purple) and F444W (orange) flux densities of AF Lep b from December 2021 to January 2024, normalized to the average flux density in each filter. All photometry at these wavelengths is consistent within 1σ with no evidence for large (>20%) variability. Top right: Retrieved emission spectra of AF Lep b (blue), compared against its L' and F444W photometry. The best-fit model is shown with the thick line, while thin lines denote 100 random emission spectra generated from the retrieved posteriors. Bottom: Comparison of retrieved parameters for $\log(P_{\text{quench}})$ (left), [Fe/H] (center), and T_{eff} (right) between our updated retrieval, which includes F444W and new L' photometry, and the previous equivalent retrieval in Zhang et al. (2023). T_{eff} and [Fe/H] produce similar posteriors, while the uncertainty on $\log(P_{\text{quench}})$, which parameterizes disequilibrium chemistry, decreases substantially.

vertical mixing, while low values of K_{zz} imply weaker mixing.

Figure 2 (top) compares the L-F444W color and effective temperature of AF Lep b to Bobcat and Elf Owl models with $\log g = 3.5 \,\mathrm{dex}$; C/O = 0.458 (corresponding to solar; Lodders & Palme 2009); and [M/H] = +0.5, 0, and -0.5. The surface gravity is selected to match the inferred log q of AF Lep b of \sim 3.7 dex from Palma-Bifani et al. (2024) and Zhang et al. (2023), while the C/O ratio and metallicity enable the inclusion of Bobcat models, which span a smaller range of metallicities and have limited coverage for non-solar C/O ratios. Within the Elf Owl models, K_{zz} varies from 10^2 to 10^9 cm² s⁻¹. For the effective temperature of AF Lep b, we adopt a nominal value of $800 \pm 100 \,\mathrm{K}$ based on effective temperatures from forward modeling ($\sim 750 \,\mathrm{K}$; Palma-Bifani et al. 2024) and retrieval ($\approx 800 \,\mathrm{K}$; Zhang et al. 2023 and this work) analyses. As expected, models with lower values of $\log K_{zz}$ corresponding to less vigorous vertical mixing have bluer L'-F444W colors, with equilibrium models

at the far blue end. This reflects the increase in CO abundance with more vigorous mixing at these effective temperatures, where faster mixing inhibits the conversion of CO to CH₄. However, as discussed by Mukherjee et al. (2024), increased $K_{\rm zz}$ is degenerate with increased atmospheric metallicity in the 3–5 μ m regime, which also increases CO abundance relative to CH₄. This is seen in Figure 2 (top), where higher-metallicity models generally produce lower L'-F444W colors at a given $T_{\rm eff}$ and $\log K_{zz}$.

The blue L'-F444W color of AF Lep b is inconsistent with sub-solar metallicity models, consistent within 1σ of solar-metallicity Elf Owl models with the most vigorous mixing $\log K_{zz} = 9$, and consistent with $[\mathrm{M/H}] = +0.5$ models with relatively high mixing levels ($\log K_{zz} = 7$ or $\log K_{zz} = 8$). Figure 2 (bottom) compares model spectra against the L' and F444W photometry of AF Lep b. Each model spectrum is anchored to the weighted mean of the L' photometry, with synthesized F444W photometry shown in open circles. The

left panel shows models varying $\log K_{\rm zz}$ and metallicity, while the right panel shows models varying metallicity with $\log K_{\rm zz}=2$. In general, the F444W photometry is best reproduced by models with high values of $\log K_{zz}$ and slightly enhanced or solar metallicites ([M/H] = 0 or [M/H] = +0.5) or lower values of $\log K_{zz}$ with supersolar metallicities ([M/H] = +1). Note that Bobcat models do not extend to metallicities of +1.0 dex. However, even with $\log K_{\rm zz}=2$ Elf Owl models, the synthesized F444W photometry remains above the observed values. This is clear evidence for the presence of disequilibrium carbon chemistry in the atmosphere of AF Lep b.

However, degeneracies remain between the metallicity enhancement and the rate of vertical mixing driving disequilibrium chemistry, both of which our observations support. The $4.3 \,\mu\mathrm{m}$ CO₂ feature can help to break this degeneracy, as CO₂ abundance is enhanced by increased metallicity, but is only weakly enhanced by disequilibrium processes (Mukherjee et al. 2024). Followup medium-band JWST photometry or M-band photometry that only samples CO₂ or CO absorption may enable more robust constraints to be placed on atmospheric metallicity and $\log K_{zz}$ within this spectral region. Another limitation of this analysis is that Bobcat and Elf Owl models are cloudless. Clouds likely affect the spectrum of AF Lep b, although the impact at these wavelengths is significantly less than at shorter wavelengths and smaller in this regime than the presence of disequilibrium chemistry (see Figure 6 of Zhang et al. 2023).

3.2.2. Updated Retrieval

To further assess the impact of the new $4.4 \,\mu\mathrm{m}$ photometry, we perform an updated retrieval following Zhang et al. (2023). Within this framework, petitradtrans (Mollière et al. 2019) is used to perform chemically-consistent retrievals. A novel temperaturepressure (T-P) profile parameterization is adopted in which the T-P profile is anchored to six temperature gradients evenly spaced across the logarithmic pressure scale. Priors on the temperature gradients informed by forward model T-P profiles are adopted to enforce radiative convective equilibrium and avoid retrievals preferring more isothermal, less cloudy T-P profiles than expected (e.g., Mollière et al. 2020; Whiteford et al. 2023). Disequilibrium chemistry follows a different parameterization than the forward models in Section 3.2.1: the logarithmic quench pressure $log(P_{quench})$ is included as a free parameter. For pressures below P_{quench} , the abundances of H_2O , CO, and CH_4 are set to their abundances at P_{quench} (e.g., Zahnle & Marley 2014). In this way, P_{quench} represents the amount of the atmosphere affected by disequilibrium chemistry, with higher values of P_{quench} indicating a larger extent of the atmospheric profile with abundances impacted by vertical mixing. See Zhang et al. (2023) and Mollière et al. (2019) for additional details on the retrieval framework.

We perform a retrieval incorporating all photometry and spectroscopy of AF Lep b from Franson et al. (2023), De Rosa et al. (2023), Mesa et al. (2023), and this work. Free parameters include the temperature at the bottom layer of the pressure profile T_{bottom} ; T-P gradients at six pressure levels $(d \ln T/d \ln P)_{1...6}$; metallicity (defined as [Fe/H]); C/O ratio; $log(P_{quench})$ [bar]; mass fractions at the base pressure $(\log(X_0))$ and sedimentation efficiencies (f_{sed}) for MgSiO₃, Fe, and KCl clouds; $\log K_{zz}$; the width of the log-normal cloud particle size distribution σ_q ; $\log(q)$; radius R; and flux offsets for the SPHERE/IFS spectra from De Rosa et al. (2023) and Mesa et al. (2023) ($\Delta f_{\rm D23}$ and $\Delta f_{\rm M23}$, respectively). Note that here, disequilibrium chemistry is not coupled to $\log K_{zz}$: the eddy diffusion coefficient is solely used to set the cloud particle size distribution, while $\log(P_{\text{quench}})$ determines non-equilibrium abundances (Mollière et al. 2020). We follow Zhang et al. (2023) in setting priors for these free parameters. The priors for all parameters other than $\log(q)$ and R can be found in Table 5 of Zhang et al. (2023). For R, a uniform prior from $1.20 R_{\text{Jup}}$ to $1.55 R_{\text{Jup}}$ is applied, informed by evolutionary models (Zhang et al. 2023). This avoids the small radius problem that has been a recurrent issue with retrievals (e.g., Kitzmann et al. 2020; Lueber et al. 2022). The log(g) prior is inferred through the radius prior and dynamical mass from Zhang et al. (2023) of $2.8 \pm 0.6 M_{\rm Jup}$. These constrained priors were also applied for some of the retrievals presented in Zhang et al. (2023).

The updated retrieval produces the following meters: [Fe/H]= $1.67^{+0.17}_{-0.20}$, $\log(L_{\rm bol}/L_{\odot})=-5.194^{+0.022}_{-0.024}$, posteriors for key parameters: $C/O=0.65^{+0.07}_{-0.09},$ $log(g)=3.65^{+0.04}_{-0.05},$ $\log(g) = 3.65^{+0.04}_{-0.05}, \quad R = 1.27^{+0.07}_{-0.05} R_{\rm Jup}, \quad T_{\rm eff} = 801^{+16}_{-20} \, {\rm K},$ and $\log(P_{\rm quench}) = 2.80^{+0.13}_{-0.26}$. These results can be discontinuous rectly compared against the rightmost column of Table 6 in Zhang et al. (2023). All parameters are consistent within 1σ with the prior retrieval. Figure 3 (bottom) compares the distributions of $log(P_{quench})$, [Fe/H], and $T_{\rm eff}$ between the two retrievals. The $T_{\rm eff}$ and [Fe/H] posteriors are similar, with our updated retrieval still finding an enhanced atmospheric metallicity. The [Fe/H] posterior corresponds to a metallicity enrichment of $Z_{\rm pl}/Z_* = 50^{+60}_{-30}$. Here, we compute $Z_{\rm pl}/Z_*$ from Equations 19 and 20 of Nasedkin et al. (2024) following the same assumptions as Thorngren & Fortney

(2019) for a host-star metallicity of -0.27 ± 0.32 (Zhang et al. 2023). This value is higher than the predicted metallicity enrichment for planets with the mass of AF Lep b; the empirical mass-metallicity relation from Thorngren et al. (2016) predicts $Z_{\rm pl}/Z_* = 6.1^{+1.2}_{-1.1}$ for a $2.8^{+0.6}_{-0.5} M_{\text{Jup}}$ planet. Note, though, that forward modeling analysis of AF Lep b has produced more modest metallicity enhancements ([Fe/H] $\approx +0.6$; Palma-Bifani et al. 2024). The main difference between the retrievals is that the $log(P_{quench})$ posterior is better constrained within the updated retrieval; the previous retrieval found $\log P_{\text{quench}} = 2.5^{+0.3}_{-1.1}$, while the updated retrieval produces a posterior of $2.80^{+0.13}_{-0.26}$. Overall, extending the SED of AF Lep b to $4.4\,\mu\mathrm{m}$ enables more precise constraints on the interior dynamics of the atmosphere of AF Lep b through sampling the carbon disequilibrium chemistry. The new photometry also affirms previous evidence for enhanced atmospheric metallicity.

3.3. Variability

Rotationally-modulated near-infrared variability is ubiquitous among isolated brown dwarf- and planetarymass objects. L and T dwarfs exhibit variability with typical amplitudes of 0.2–5% from 1–5 μ m (e.g., Artigau et al. 2009; Metchev et al. 2015; Biller et al. 2018; Zhou et al. 2020), although amplitudes up to 38% in J band have been observed (Bowler et al. 2020; Zhou et al. 2022). The primary source of this variability, at least for late-L- and T-type objects, is likely heterogeneous clouds (e.g., Apai et al. 2013; Morley et al. 2014; Vos et al. 2023; McCarthy et al. 2024). In line with this interpretation, variability amplitudes and occurrence rates are higher at young ages (Vos et al. 2022), the L/T transition (Radigan et al. 2014), and equatoron viewing angles (Vos et al. 2017). These trends bode well for the potential to use photometric variability to characterize directly imaged planets. Moreover, Jupiter exhibits disk-averaged variability of $\sim 4\%$ in the optical and $\sim 20\%$ at 4.7 μ m (Gelino & Marley 2000; Ge et al. 2019). However, despite several attempts (Apai et al. 2016; Biller et al. 2021; Wang et al. 2022), variability has yet to be detected for resolved, imaged exoplanets on closer-in (<100 au) orbits, where photometric precision is limited by PSF subtraction.

The two epochs of F444W photometry and three epochs of L' photometry of AF Lep b do not show evidence of variability at the 10% and 20% levels, respectively. Figure 3 (top left) displays the flux densities of the L' and F444W photometry of AF Lep b, normalized to the average flux density for each filter. All photometry is consistent within 1σ . The F444W photometry has an average flux density of

 $(2.96\pm0.28)\times10^{-18}\,\mathrm{erg/s/cm^2/\mathring{A}}$. The two epochs separated by three months differ by $0.2\pm0.6\,\mathrm{erg/s/cm^2/\mathring{A}}$ or $0.06\pm0.23\,\mathrm{mag}$. Here, the 1.5% absolute flux calibration uncertainty is not included, as a NIRCam flux offset would have a uniform effect on both photometric points. The average L' flux density is $(5.8\pm0.6)\times10^{-18}\,\mathrm{erg/s/cm^2/\mathring{A}}$. Each L' point, spanning a baseline of two years, is consistent within 1σ of the average. The ratio of the standard deviation of all photometric points to the mean photometric uncertainty, $\sigma/\overline{\sigma}_{\rm meas}$, offers a way to compare the significance level of potential variability signals. Here, $\sigma/\overline{\sigma}_{\rm meas}\gg1$ indicates variability, while $\sigma/\overline{\sigma}_{\rm meas}\lesssim1$ indicates no evidence for variability. This ratio is 0.3 for F444W and 0.54 for L'.

4. SUMMARY

In this work, we presented JWST/NIRCam imaging of the $3\,M_{\rm Jup}$ planet AF Lep b. AF Lep b is recovered at a significance of 9.6σ and 8.7σ in two epochs of F444W NIRcam imaging. This extends the SED of this recently discovered planet into the 4– $5\,\mu{\rm m}$ regime. We also presented new Keck/NIRC2 L' imaging of AF Lep b. Our main conclusions are summarized below:

- AF Lep b is relatively faint in F444W, with an average flux density 51% of its average flux density in L', indicating significant CO absorption. At the effective temperature of AF Lep b, this points to the presence of disequilibrium carbon chemistry driven by vertical mixing. Enhanced atmospheric metallicity also increases CO abundance, although at [M/H]= +0.5, only forward models with vigorous vertical mixing (log K_{zz} > 4) are consistent with the observed 3–5 μm photometry.
- An updated retrieval within the Zhang et al. (2023) framework produces consistent posteriors with the previous retrieval for most parameters. The uncertainty on the quench pressure (log(P_{quench})), which is used to parameterize disequilibrium chemistry, decreases significantly. An enhancement in the atmospheric metallicity is still found. Overall, the F444W photometry provides clear evidence for disequilibrium chemistry within the atmosphere of AF Lep b while affirming previous evidence for enhanced atmospheric metallicity.
- No additional planets on wider orbits are detected around AF Lep. Our F444W contrast curve places deep upper limits on the mass of additional companions in the system, ruling out $1.9\,M_{\rm Jup}$ planets beyond 0".5, $1.1\,M_{\rm Sat}$ planets beyond 1", and $2.8\,M_{\rm Nep}$ planets beyond 2".5. This largely rules

out the scenario of an additional giant planet sculpting the debris disk around AF Lep.

The successful imaging of AF Lep b with JWST at its current separation of $\approx 320\,\mathrm{mas}$ and F444W contrast of $\approx 10\,\mathrm{mag}$ is an exciting technical achievment. Alongside the recent MIRI (Boccaletti et al. 2023) detection of HR 8799 e at a separation of 350 mas, our recovery of AF Lep b demonstrates that JWST coronagraphy is outperforming pre-launch expectations at close-in separations.

5. ACKNOWLEDGEMENTS

We greatly appreciate the efforts of the JWST mission operations team for rapidly scheduling this DD program. K.F. acknowledges support from the National Science Foundation Graduate Research Fellowship Program under Grant No. DGE 2137420. B.P.B. acknowledges support from the National Science Foundation grant AST-1909209, NASA Exoplanet Research Program grant 20-XRP20_2-0119, and the Alfred P. Sloan Foundation. T.D.P is supported by a UKRI/EPSRC Stephen Hawking Fellowship. This work is based on observations made with the NASA/ESA/CSA James Webb Space Telescope. The data were obtained from the Mikulski Archive for Space Telescopes at the Space Telescope Science Institute, which is operated by the Association of Universities for Research in Astronomy, Inc., under NASA contract NAS 5-03127 for JWST. These observations are associated with program #4558. Support for program #4558 was provided by NASA through a grant from the Space Telescope Science Institute, which is operated by the Association of Universities for Research in Astronomy, Inc., under NASA contract NAS 5-03127. This research has made use of the VizieR catalogue access tool, CDS, Strasbourg, France (DOI: 10.26093/cds/vizier). The original description of the VizieR service was published in 2000, A&AS 143, 23. This publication makes use of data products from the Wide-field Infrared Survey Explorer, which is a joint project of the University of California, Los Angeles, and the Jet Propulsion Laboratory/California Institute of Technology, funded by the National Aeronautics and Space Administration. Based on observations made with ESO Telescopes at the La Silla Paranal Observatory under programme ID 2111.C-5021(B). This work was supported by a NASA Keck PI Data Award, administered by the NASA Exoplanet Science Institute. Data presented herein were obtained at the W. M. Keck Observatory from telescope time allocated to the National Aeronautics and Space Administration through the agency's scientific partnership with the California Institute of Technology and the University of California. The Observatory was made possible by the generous financial support of the W. M. Keck Foundation.

The authors wish to recognize and acknowledge the very significant cultural role and reverence that the summit of Maunakea has always had within the indigenous Hawaiian community. We are most fortunate to have the opportunity to conduct observations from this mountain.

Software: pyKLIP (Wang et al. 2015), spaceKLIP (Kammerer et al. 2022), pysynphot (STScI Development Team 2013), webbpsf (Perrin et al. 2012, 2014), ccdproc (Craig et al. 2017), photutils (Bradley et al. 2019), astropy (Astropy Collaboration et al. 2013, 2018), pandas (McKinney 2010), matplotlib (Hunter 2007), numpy (Harris et al. 2020), scipy (Virtanen et al. 2020), emcee (Foreman-Mackey et al. 2013), corner (Foreman-Mackey 2016)

APPENDIX

A. ADDITIONAL JWST AND KECK/NIRC2 IMAGING

In this section, we present additional reduced frames from the JWST and Keck/NIRC2 datasets not shown in Figure 2. Figure 4 displays the F200W and F356W imaging in which AF Lep b is not detected at a significant level (top and middle rows), full-frame F444W imaging (bottom row, center and left), and the January 2024 Keck/NIRC2 L' imaging (bottom row, right). A speckle appears in both F356W datasets at the expected position of AF Lep b. However, the S/N of these speckles (3.7 σ and 3.2 σ in October 2023 and January 2024, respectively) falls below our nominal cutoff (5 σ) for claiming a detection. No significant sources are seen in the F200W imaging. The effect of the pointing error in the January 2024 data, which is in the SE direction from the mask center, can be seen in the January 2024 F200W imaging. No significant point sources are seen at wider separations in the full-frame F444W imaging. The source at (Δ RA, Δ Dec) \approx (1"2, 5") in the October imaging is a cosmic ray "snowball" artifact (see e.g., Bagley et al. 2023) that does not appear in the January observations.

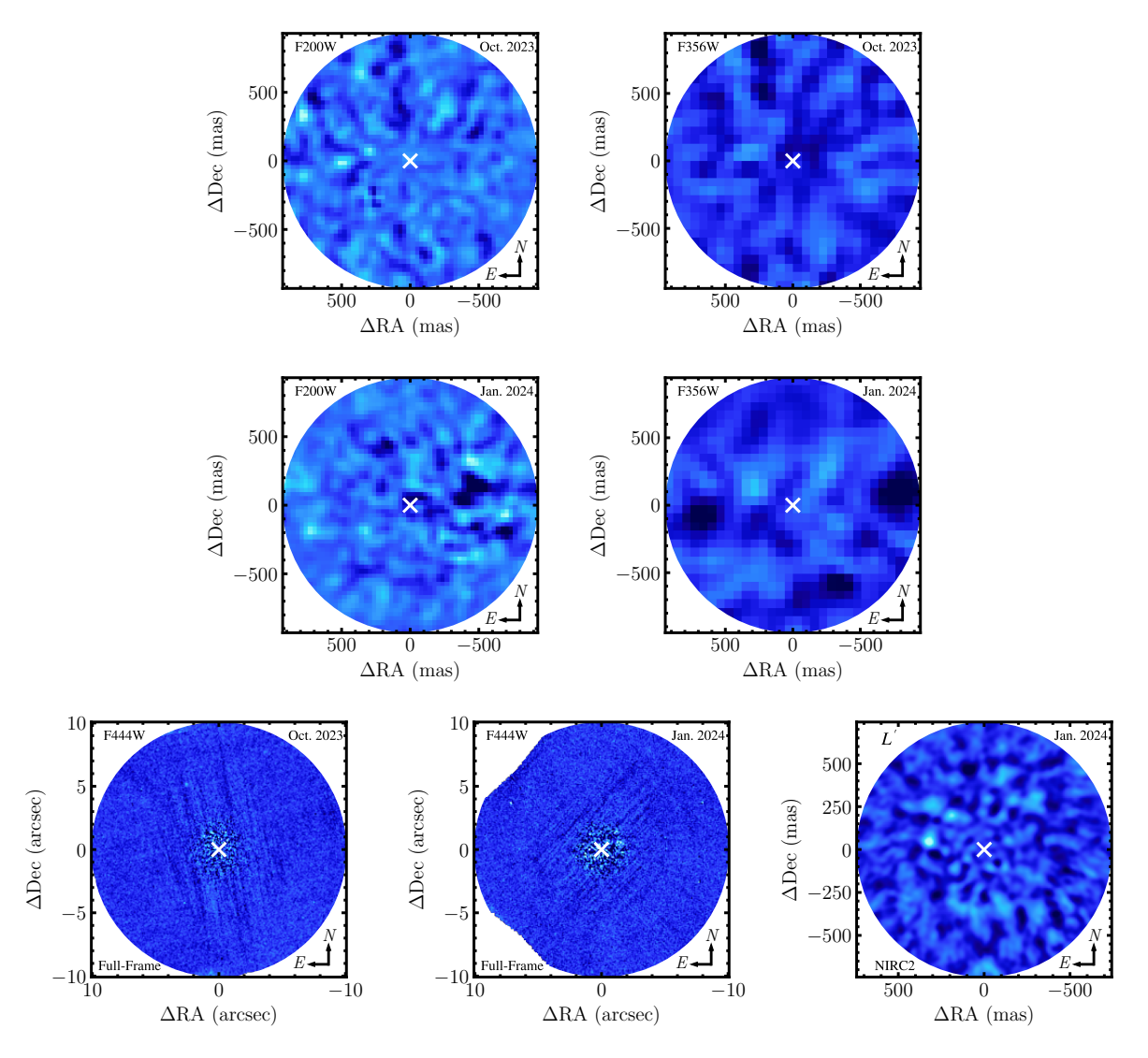


Figure 4. Top and Middle: F200W (left) and F356W (right) imaging of AF Lep. AF Lep b is not robustly recovered ($>5\sigma$) in either filter or epoch. Like the F444W imaging in Figure 1, each image is convolved with a Gaussian filter with a standard deviation of 1 pixel. Bottom: The left and center panels show full-frame F444W imaging of AF Lep for each sequence. No significant point sources are seen at wider separations in this imaging. The artifact to the NE of the star in the October 2023 imaging is a cosmic ray artifact that does not appear in the January 2024 imaging. The right panel shows our new Keck/NIRC2 L' imaging of AF Lep b. To smooth over pixel-to-pixel noise, the image is convolved with a Gaussian filter with a standard deviation of 1.5 pixels. AF Lep b is recovered at a S/N of 6.6σ .

Acton, D. S., Knight, J. S., Contos, A., et al. 2012, in SPIE
Astronomical Telescopes + Instrumentation, ed. M. C.
Clampin, G. G. Fazio, H. A. MacEwen, & J. M.
Oschmann, Amsterdam, Netherlands, 84422H,
doi: 10.1117/12.925015

Apai, D., Radigan, J., Buenzli, E., et al. 2013, The Astrophysical Journal, 768, 121,

doi: 10.1088/0004-637X/768/2/121

Apai, D., Kasper, M., Skemer, A., et al. 2016, ApJ, 820, 40, doi: 10.3847/0004-637X/820/1/40

Artigau, É., Bouchard, S., Doyon, R., & Lafrenière, D. 2009, The Astrophysical Journal, 701, 1534, doi: 10.1088/0004-637X/701/2/1534

Astropy Collaboration, Robitaille, T. P., Tollerud, E. J., et al. 2013, A&A, 558, A33, doi: 10.1051/0004-6361/201322068

- Astropy Collaboration, Price-Whelan, A. M., Sipőcz, B. M., et al. 2018, AJ, 156, 123, doi: 10.3847/1538-3881/aabc4f
- Atreya, S. K., Mahaffy, P. R., Niemann, H. B., Wong,
 M. H., & Owen, T. C. 2003, Planetary and Space
 Science, 51, 105, doi: 10.1016/S0032-0633(02)00144-7
- Bagley, M. B., Finkelstein, S. L., Koekemoer, A. M., et al. 2023, ApJL, 946, L12, doi: 10.3847/2041-8213/acbb08
- Barman, T. S., Macintosh, B., Konopacky, Q. M., & Marois, C. 2011, ApJ, 733, 65, doi: 10.1088/0004-637X/733/1/65
- Bell, C. P. M., Mamajek, E. E., & Naylor, T. 2015, MNRAS, 454, 593, doi: 10.1093/mnras/stv1981
- Beuzit, J.-L., Vigan, A., Mouillet, D., et al. 2019, A&A, 631, A155, doi: 10.1051/0004-6361/201935251
- Biller, B. A., Vos, J., Buenzli, E., et al. 2018, AJ, 155, 95, doi: 10.3847/1538-3881/aaa5a6
- Biller, B. A., Apai, D., Bonnefoy, M., et al. 2021, Monthly Notices of the Royal Astronomical Society, 503, 743, doi: 10.1093/mnras/stab202
- Boccaletti, A., Mâlin, M., Baudoz, P., et al. 2023, arXiv e-prints, arXiv:2310.13414, doi: 10.48550/arXiv.2310.13414
- Bohlin, R. C., Mészáros, S., Fleming, S. W., et al. 2017,
 The Astronomical Journal, 153, 234,
 doi: 10.3847/1538-3881/aa6ba9
- Bonnefoy, M., Marleau, G. D., Galicher, R., et al. 2014, Astronomy and Astrophysics, 567, L9, doi: 10.1051/0004-6361/201424041
- Bowler, B. P., Liu, M. C., Dupuy, T. J., & Cushing, M. C. 2010, The Astrophysical Journal, 723, 850, doi: 10.1088/0004-637X/723/1/850
- Bowler, B. P., Liu, M. C., Shkolnik, E. L., & Dupuy, T. J. 2013, ApJ, 774, 55, doi: 10.1088/0004-637X/774/1/55
- Bowler, B. P., Zhou, Y., Morley, C. V., et al. 2020, The Astrophysical Journal, 893, L30, doi: 10.3847/2041-8213/ab8197
- Bradley, L., Sipőcz, B., Robitaille, T., et al. 2019, Astropy/Photutils: V0.7.2, Zenodo, doi: 10.5281/zenodo.3568287
- Brandt, T. D. 2021, ApJS, 254, 42, doi: 10.3847/1538-4365/abf93c
- Burrows, A., Hubbard, W. B., Lunine, J. I., & Liebert, J. 2001, RvMP, 73, 719, doi: 10.1103/RevModPhys.73.719
- Bushouse, H., Eisenhamer, J., Dencheva, N., et al. 2023, JWST Calibration Pipeline, 1.12.1, Zenodo, Zenodo, doi: 10.5281/zenodo.6984365
- Carter, A. L., Hinkley, S., Bonavita, M., et al. 2021, MNRAS, 501, 1999. http://ascl.net/2011.07075
- Carter, A. L., Hinkley, S., Kammerer, J., et al. 2023, ApJL, 951, L20. http://ascl.net/2208.14990

- Chauvin, G., Lagrange, A.-M., Dumas, C., et al. 2004, A&A, 425, L29, doi: 10.1051/0004-6361:200400056
- Chauvin, G., Desidera, S., Lagrange, A.-M., et al. 2017, Astronomy & Samp; Astrophysics, Volume 605, id.L9, <NUMPAGES>9</NUMPAGES> pp., 605, L9, doi: 10.1051/0004-6361/201731152
- Cheetham, A. C., Samland, M., Brems, S. S., et al. 2019, Astronomy and Astrophysics, 622, A80, doi: 10.1051/0004-6361/201834112
- Craig, M., Crawford, S., Seifert, M., et al. 2017, Astropy/Ccdproc: V1.3.0.Post1, Zenodo, doi: 10.5281/zenodo.1069648
- Currie, T., Burrows, A., Madhusudhan, N., et al. 2013, The Astrophysical Journal
- Cutri, R. M., Wright, E. L., Conrow, T., & et al. 2012, VizieR Online Data Catalog, II/311
- Davidson, J. W., Horch, E. P., Majewski, S. R., et al. 2024,
 The Astronomical Journal, 167, 117,
 doi: 10.3847/1538-3881/ad1ff6
- De Rosa, R. J., Nielsen, E. L., Wahhaj, Z., et al. 2023, A&A, 672, A94, doi: 10.1051/0004-6361/202345877
- Faherty, J. K., Riedel, A. R., Cruz, K. L., et al. 2016, ApJS, 225, 10, doi: 10.3847/0067-0049/225/1/10
- Filippazzo, J. C., Rice, E. L., Faherty, J., et al. 2015, ApJ, 810, 158, doi: 10.1088/0004-637X/810/2/158
- Flasar, F. M., Achterberg, R. K., Conrath, B. J., et al. 2005, Science, 307, 1247, doi: 10.1126/science.1105806
- Foreman-Mackey, D. 2016, JOSS, 1, 24, doi: 10.21105/joss.00024
- Foreman-Mackey, D., Hogg, D. W., Lang, D., & Goodman, J. 2013, PASP, 125, 306, doi: 10.1086/670067
- Franson, K., Bowler, B. P., Brandt, T. D., et al. 2022, AJ, 163, 50, doi: 10.3847/1538-3881/ac35e8
- Franson, K., Bowler, B. P., Zhou, Y., et al. 2023, ApJL, 950, L19, doi: 10.3847/2041-8213/acd6f6
- Fruchter, A. S., & Hook, R. N. 2002, PASP, 114, 144, doi: 10.1086/338393
- Gaia Collaboration, Vallenari, A., Brown, A., Prusti, T., & et al. 2022, A&A, doi: 10.1051/0004-6361/202243940
- Gardner, J. P., Mather, J. C., Clampin, M., et al. 2006, Space Science Reviews, 123, 485, doi: 10.1007/s11214-006-8315-7
- Gardner, J. P., Mather, J. C., Abbott, R., et al. 2023, PASP, 135, 068001, doi: 10.1088/1538-3873/acd1b5
- Ge, H., Zhang, X., Fletcher, L. N., et al. 2019, AJ, 157, 89, doi: 10.3847/1538-3881/aafba7
- Gelino, C., & Marley, M. 2000, 212, 322
- Girard, J. H., Leisenring, J., Kammerer, J., et al. 2022, JWST/NIRCam Coronagraphy: Commissioning and First On-Sky Results. http://ascl.net/2208.00998

- Gray, R. O., Corbally, C. J., Garrison, R. F., et al. 2006, AJ, 132, 161, doi: 10.1086/504637
- Griffith, C. A., & Yelle, R. V. 1999, The Astrophysical Journal, 519, L85, doi: 10.1086/312103
- Harris, C. R., Millman, K. J., van der Walt, S. J., et al. 2020, Natur, 585, 357, doi: 10.1038/s41586-020-2649-2
- Hinz, P. M., Rodigas, T. J., Kenworthy, M. A., et al. 2010, ApJ, 716, 417, doi: 10.1088/0004-637X/716/1/417
- Høg, E., Fabricius, C., Makarov, V. V., et al. 2000, \aap, 355, L27
- Horch, E. P., Veillette, D. R., Baena Gallé, R., et al. 2009,
 The Astronomical Journal, 137, 5057,
 doi: 10.1088/0004-6256/137/6/5057
- Hunter, J. D. 2007, CSE, 9, 90, doi: 10.1109/MCSE.2007.55
- Kammerer, J., Girard, J., Carter, A. L., et al. 2022, Performance of Near-Infrared High-Contrast Imaging Methods with JWST from Commissioning. http://ascl.net/2208.00996
- Kammerer, J., Lawson, K., Perrin, M. D., et al. 2024, JWST-TST High Contrast: JWST/NIRCam Observations of the Young Giant Planet \$\beta\$ Pic b, doi: 10.3847/1538-3881/ad4ffe
- Kirkpatrick, J. D. 2005, ARA&A, 43, 195, doi: 10.1146/annurev.astro.42.053102.134017
- Kitzmann, D., Heng, K., Oreshenko, M., et al. 2020, ApJ, 890, 174, doi: 10.3847/1538-4357/ab6d71
- Knapp, G. R., Leggett, S. K., Fan, X., et al. 2004, The Astronomical Journal, 127, 3553, doi: 10.1086/420707
- Konopacky, Q. M., Barman, T. S., Macintosh, B. A., & Marois, C. 2013, Science, 339, 1398, doi: 10.1126/science.1232003
- Krist, J. E., Balasubramanian, K., Muller, R. E., et al. 2010, in Society of Photo-Optical Instrumentation
 Engineers (SPIE) Conference Series, Vol. 7731, Space
 Telescopes and Instrumentation 2010: Optical, Infrared, and Millimeter Wave, ed. Jr. Oschmann, Jacobus M.,
 M. C. Clampin, & H. A. MacEwen, 77313J,
 doi: 10.1117/12.856488
- Lafrenière, D., Marois, C., Doyon, R., & Barman, T. 2009, ApJ, 694, L148, doi: 10.1088/0004-637X/694/2/L148
- Lagrange, A.-M., Bonnefoy, M., Chauvin, G., et al. 2010, Sci, 329, 57, doi: 10.1126/science.1187187
- Lawson, K., Schlieder, J. E., Leisenring, J. M., et al. 2023, JWST/NIRCam Coronagraphy of the Young Planet-hosting Debris Disk AU Microscopii, arXiv. http://ascl.net/2308.02486
- Lindegren, L. 2018, Re-Normalising the Astrometric Chi-Square in Gaia DR2, Tech. Rep. GAIA-C3-TN-LU-LL-124-01

- Linder, E. F., Mordasini, C., Mollière, P., et al. 2019, A&A, 623, A85, doi: 10.1051/0004-6361/201833873
- Liu, M. C. 2004, Sci, 305, 1442, doi: 10.1126/science.1102929
- Liu, M. C., Dupuy, T. J., & Allers, K. N. 2016, ApJ, 833, 96, doi: 10.3847/1538-4357/833/1/96
- Lodders, K., & Palme, H. 2009, Meteoritics and Planetary Science Supplement, 72, 5154
- Lueber, A., Kitzmann, D., Bowler, B. P., Burgasser, A. J., & Heng, K. 2022, ApJ, 930, 136, doi: 10.3847/1538-4357/ac63b9
- Macintosh, B., Graham, J. R., Barman, T., et al. 2015, Science, 350, 64, doi: 10.1126/science.aac5891
- Marley, M. S., Saumon, D., Cushing, M., et al. 2012, The Astrophysical Journal, 754, 135, doi: 10.1088/0004-637X/754/2/135
- Marley, M. S., Saumon, D., Visscher, C., et al. 2021, ApJ, 920, 85, doi: 10.3847/1538-4357/ac141d
- Marois, C., Lafrenière, D., Doyon, R., Macintosh, B., & Nadeau, D. 2006, ApJ, 641, 556, doi: 10.1086/500401
- Marois, C., Macintosh, B., Barman, T., et al. 2008, Science, 322, 1348, doi: 10.1126/science.1166585
- Mawet, D., Milli, J., Wahhaj, Z., et al. 2014, ApJ, 792, 97, doi: 10.1088/0004-637X/792/2/97
- McCarthy, A. M., Muirhead, P. S., Tamburo, P., et al. 2024, Multiple Patchy Cloud Layers in the Planetary Mass Object SIMP0136+0933, arXiv, doi: 10.48550/arXiv.2402.15001
- McElwain, M. W., Feinberg, L. D., Perrin, M. D., et al. 2023, PASP, 135, 058001, doi: 10.1088/1538-3873/acada0
- McKinney, W. 2010, in Proceedings of the 9th Python in Science Conference, Austin, Texas, 56–61, doi: 10.25080/Majora-92bf1922-00a
- Mesa, D., Gratton, R., Kervella, P., et al. 2023, A&A, 672, A93, doi: 10.1051/0004-6361/202345865
- Metchev, S. A., Heinze, A., Apai, D., et al. 2015, ApJ, 799, 154, doi: 10.1088/0004-637X/799/2/154
- Mollière, P., Boekel, R. V., Dullemond, C., Henning, Th., & Mordasini, C. 2015, ApJ, 813, 47, doi: 10.1088/0004-637X/813/1/47
- Mollière, P., Wardenier, J. P., van Boekel, R., et al. 2019, Astronomy and Astrophysics, 627, A67, doi: 10.1051/0004-6361/201935470
- Mollière, P., Stolker, T., Lacour, S., et al. 2020, arXiv:2006.09394 [astro-ph]. http://ascl.net/2006.09394
- Mordasini, C., Marleau, G. D., & Mollière, P. 2017, Astronomy and Astrophysics, 608, A72, doi: 10.1051/0004-6361/201630077

- Morley, C. V., Marley, M. S., Fortney, J. J., & Lupu, R. 2014, The Astrophysical Journal, 789, L14, doi: 10.1088/2041-8205/789/1/L14
- Mukherjee, S., Fortney, J. J., Morley, C. V., et al. 2024, The Sonora Substellar Atmosphere Models. IV. Elf Owl: Atmospheric Mixing and Chemical Disequilibrium with Varying Metallicity and C/O Ratios, arXiv. http://ascl.net/2402.00756
- Nasedkin, E., Mollière, P., Lacour, S., et al. 2024, Four-of-a-Kind? Comprehensive Atmospheric Characterisation of the HR 8799 Planets with VLTI/GRAVITY, arXiv, doi: 10.48550/arXiv.2404.03776
- Oppenheimer, B. R., Kulkarni, S. R., Matthews, K., & Nakajima, T. 1995, Science, 270, 1478, doi: 10.1126/science.270.5241.1478
- Palma-Bifani, P., Chauvin, G., Borja, D., et al. 2024, Atmospheric Properties of AF Lep b with Forward Modeling, arXiv. http://ascl.net/2401.05491
- Pawellek, N., Wyatt, M., Matrà, L., Kennedy, G., & Yelverton6, B. 2021, Monthly Notices of the Royal Astronomical Society, 502, 5390, doi: 10.1093/mnras/stab269
- Pearce, T. D., Launhardt, R., Ostermann, R., et al. 2022, A&A, 659, A135, doi: 10.1051/0004-6361/202142720
- Perrin, M. D., Sivaramakrishnan, A., Lajoie, C.-P., et al. 2014, in Society of Photo-Optical Instrumentation
 Engineers (SPIE) Conference Series, Vol. 9143, Space
 Telescopes and Instrumentation 2014: Optical, Infrared, and Millimeter Wave, ed. Jr. Oschmann, Jacobus M.,
 M. Clampin, G. G. Fazio, & H. A. MacEwen, 91433X, doi: 10.1117/12.2056689
- Perrin, M. D., Soummer, R., Elliott, E. M., Lallo, M. D., & Sivaramakrishnan, A. 2012, in Society of Photo-Optical Instrumentation Engineers (SPIE) Conference Series,
 Vol. 8442, Space Telescopes and Instrumentation 2012:
 Optical, Infrared, and Millimeter Wave, ed. M. C.
 Clampin, G. G. Fazio, H. A. MacEwen, & Jr. Oschmann,
 Jacobus M., 84423D, doi: 10.1117/12.925230
- Phillips, M. W., Tremblin, P., Baraffe, I., et al. 2020, A&A, 637, A38, doi: 10.1051/0004-6361/201937381
- Pueyo, L. 2016, ApJ, 824, 117, doi: 10.3847/0004-637X/824/2/117
- Radigan, J., Lafrenière, D., Jayawardhana, R., & Artigau,
 E. 2014, ApJ, 793, 75, doi: 10.1088/0004-637X/793/2/75
- Rajan, A., Rameau, J., Rosa, R. J. D., et al. 2017, AJ, 154, 10, doi: 10.3847/1538-3881/aa74db

- Rebollido, I., Stark, C. C., Kammerer, J., et al. 2024, JWST-TST High Contrast: Asymmetries, Dust Populations and Hints of a Collision in the \$\beta\$ Pictoris Disk with NIRCam and MIRI, arXiv. http://ascl.net/2401.05271
- Rieke, M. J., Kelly, D., & Horner, S. 2005, in Optics & Photonics 2005, ed. J. B. Heaney & L. G. Burriesci, San Diego, California, USA, 590401, doi: 10.1117/12.615554
- Rieke, M. J., Kelly, D. M., Misselt, K., et al. 2023, PASP, 135, 028001, doi: 10.1088/1538-3873/acac53
- Rigby, J., Perrin, M., McElwain, M., et al. 2023, PASP, 135, 048001, doi: 10.1088/1538-3873/acb293
- Sanghi, A., Liu, M. C., Best, W. M. J., et al. 2023, The Astrophysical Journal, 959, 63, doi: 10.3847/1538-4357/acff66
- Service, M., Lu, J. R., Campbell, R., et al. 2016, PASP, 128, 095004, doi: 10.1088/1538-3873/128/967/095004
- Skemer, A. J., Hinz, P. M., Esposito, S., et al. 2012, ApJ, 753, 14, doi: 10.1088/0004-637X/753/1/14
- Skemer, A. J., Marley, M. S., Hinz, P. M., et al. 2014, ApJ, 792, 17, doi: 10.1088/0004-637X/792/1/17
- Skrutskie, M. F., Cutri, R. M., Stiening, R., et al. 2006, AJ, 131, 1163, doi: 10.1086/498708
- Soummer, R., Pueyo, L., & Larkin, J. 2012, ApJ, 755, L28, doi: 10.1088/2041-8205/755/2/L28
- Stolker, T., Quanz, S. P., Todorov, K. O., et al. 2020, A&A, 635, A182, doi: 10.1051/0004-6361/201937159
- STScI Development Team. 2013, Astrophysics Source Code Library, ascl:1303.023
- Thorngren, D., & Fortney, J. J. 2019, ApJL, 874, L31, doi: 10.3847/2041-8213/ab1137
- Thorngren, D. P., Fortney, J. J., Murray-Clay, R. A., & Lopez, E. D. 2016, ApJ, 831, 64, doi: 10.3847/0004-637X/831/1/64
- Tokovinin, A. 2023, Exploring Thousands of Nearby Hierarchical Systems with Gaia and Speckle Interferometry, arXiv. http://ascl.net/2303.17620
- Tsuji, T., Ohnaka, K., Aoki, W., & Nakajima, T. 1996, Astronomy and Astrophysics, 308, L29
- van Dokkum, P. G. 2001, PASP, 113, 1420, doi: 10.1086/323894
- Virtanen, P., Gommers, R., Oliphant, T. E., et al. 2020, Nature Methods, 17, 261, doi: 10.1038/s41592-019-0686-2
- Vos, J. M., Allers, K. N., & Biller, B. A. 2017, ApJ, 842, 78, doi: 10.3847/1538-4357/aa73cf
- Vos, J. M., Faherty, J. K., Gagné, J., et al. 2022, ApJ, 924, 68, doi: 10.3847/1538-4357/ac4502
- Vos, J. M., Burningham, B., Faherty, J. K., et al. 2023, The Astrophysical Journal, 944, 138, doi: 10.3847/1538-4357/acab58

- Wang, J. J., Ruffio, J.-B., De Rosa, R. J., et al. 2015, pyKLIP: PSF Subtraction for Exoplanets and Disks, Astrophysics Source Code Library, record ascl:1506.001. http://ascl.net/1506.001
- Wang, J. J., Graham, J. R., Pueyo, L., et al. 2016, The Astronomical Journal, 152, 97, doi: 10.3847/0004-6256/152/4/97
- Wang, J. J., Gao, P., Chilcote, J., et al. 2022, Atmospheric Monitoring and Precise Spectroscopy of the HR 8799 Planets with SCExAO/CHARIS. http://ascl.net/2208.05594
- Whiteford, N., Glasse, A., Chubb, K. L., et al. 2023, Retrieval Study of Cool, Directly Imaged Exoplanet 51 Eri b, arXiv. http://ascl.net/2302.07939

- Wizinowich, P. 2013, PASP, 125, 798, doi: 10.1086/671425
 Zahnle, K. J., & Marley, M. S. 2014, The Astrophysical Journal, 797, 41, doi: 10.1088/0004-637X/797/1/41
 Zhang, Z. 2024, Research Notes of the AAS, 8, 114,
- Zhang, Z., Mollière, P., Hawkins, K., et al. 2023, AJ, 166, 198. http://ascl.net/2309.02488

doi: 10.3847/2515-5172/ad4481

- Zhou, Y., Bowler, B. P., Apai, D., et al. 2022, Roaring Storms in the Planetary-Mass Companion VHS
 1256-1257 b: Hubble Space Telescope Multi-epoch Monitoring Reveals Vigorous Evolution in an Ultra-cool Atmosphere, arXiv. http://ascl.net/2210.02464
- Zhou, Y., Bowler, B. P., Morley, C. V., et al. 2020, The Astronomical Journal, 160, 77, doi: 10.3847/1538-3881/ab9e04